Mechanics of Advanced Materials and Structures

ISSN: (Print) (Online) Journal homepage: https://www.tandfonline.com/loi/umcm20

Bending behavior of triply periodic minimal surface foam-filled tubes

Nejc Novak, Oraib Al-Ketan, Lovre Krstulović-Opara, Reza Rowshan, Matej Vesenjak & Zoran Ren

To cite this article: Nejc Novak, Oraib Al-Ketan, Lovre Krstulović-Opara, Reza Rowshan, Matej Vesenjak & Zoran Ren (2022): Bending behavior of triply periodic minimal surface foam-filled tubes, Mechanics of Advanced Materials and Structures, DOI: 10.1080/15376494.2022.2068207

To link to this article: https://doi.org/10.1080/15376494.2022.2068207

Published online: 27 Apr 2022.

MECHANICS OF ADVANCED MATERIALS AND STRUCTURES
https://doi.org/10.1080/15376494.2022.2068207

Taylor & Francis
Taylor & Francis Group

ORIGINAL ARTICLE

Bending behavior of triply periodic minimal surface foam-filled tubes

Nejc Novak[a], Oraib Al-Ketan[b], Lovre Krstulović-Opara[c], Reza Rowshan[b], Matej Vesenjak[a], and Zoran Ren[a]

[a]Faculty of Mechanical Engineering, University of Maribor, Maribor, Slovenia; [b]Core Technology Platforms Operations, New York University Abu Dhabi, Abu Dhabi, UAE; [c]Faculty of Electrical Engineering, Mechanical Engineering and Naval Architecture, University of Split, Split, Croatia

ABSTRACT

Foam-filled tubes represent one of the best energy-absorbing components for future crashworthiness applications. Triply Periodic Minimal Surface (TPMS)-filled tubes were investigated under quasi-static and dynamic three-point bending loading conditions. The TPMS-filled tubes enhanced specific energy absorption up to 46% compared to the sum of empty tubes and the core response separately. The validated computational models were used to extend the computational study to investigate graded core of TPMS-filled tubes under bending loading. The study results show that the mechanical response of TPMS-filled tubes can be tuned using different relative densities or/and distributions of relative density of the core.

ARTICLE HISTORY
Received 24 January 2022
Accepted 17 April 2022

KEYWORDS
Foams; foam-filled tubes; mechanical testing; computational modeling; mechanical properties; bending

Introduction

The foam-filled tubes are one of the best energy-absorbing components in the field of crashworthiness, blast and impact protection due to their lightweight design and extraordinary energy absorption capabilities. The majority of protective structures are subjected to bending loading, where the cross-sectional arrangement of the material significantly influences their behavior. The cores of foam-filled tubes can consist of different cellular or composite materials, providing different mechanical properties and deformation modes. The core materials can be arranged to have less dense material in regions with low bending loads and higher density in heavily loaded regions.

Several studies of foam-filled tube behavior under mechanical loading, mainly axial compression loading, have been conducted [1]. It has been shown that the *ex-situ* [2] and *in-situ* [3] aluminum foam-filled tubes improve crush performance under axial compressive loads if compared to empty tubes. The *in-situ* and *ex-situ* aluminum matrix foam-filled tubes were recently fabricated using inert gas pressure infiltration and tested under compression loading, where the in-situ foam-filled tubes perform better than the ex-situ-filled tubes [4]. The improved compression performance of Advanced Pore Morphology (APM) foam-filled tubes was evaluated in [5]. It was shown that the polyamide-bonded APM foam-filled tubes are comparable to the conventional foam-filled tubes showing a similar compressive stress-strain relationship. However, the Specific Energy Absorption (SEA) is higher if compared to the conventional foam-filled tubes. A step further introduces the silicon filler in the open-cell foam core, which results in a polymer-aluminum alloy hybrid foam used as a core for foam-filled tubes [6]. An increase of specific energy absorption up to 78% of hybrid foam-filled structures compared to the empty tubes was noted. The study of the tube material influence on the mechanical response of foam-filled aluminum tubes at different temperatures showed that the deformation mode is changed at elevated temperatures and that the 6061-T6 alloy exhibits better energy absorption capacities [7]. The foam-filled tubes are also one of the best candidates for energy absorption in case of a vehicle crash [8].

Furthermore, the core geometry could also be adapted to the specific loads, as shown in [9], where the aluminum tubes filled with bioinspired cores of closed-cell aluminum foam were studied. The results showed that 9 of 12 bionic samples had higher energy absorption capacity than the corresponding fully-filled samples. The introduction of auxetic cores with negative Poisson's ratio has shown that the auxetic foam-filled square tube is superior to empty and conventional foam-filled square tubes in terms of all studied crashworthiness indicators [10, 11].

Recent advances in additive manufacturing enable the fabrication of very complex cellular geometries like Triply Periodical Minimal Surface (TPMS) cellular structures [12–18]. Al-Ketan et al. [12] showed that the sheet-based TPMS structures exhibit enhanced mechanical properties compared to the strut-based TPMS lattices and other conventional strut-based lattices, such as the octet-truss and the Kelvin unit cells. Other lattices, such as functionally graded TPMS lattices [19] and honeycomb Gyroid [20], have also been derived from TPMS lattices. Surface-based TPMS cellular structures could also be used for advanced foam-filled tubes, i.e., TPMS-filled tubes, which were recently studied

CONTACT Nejc Novak n.novak@um.si Faculty of Mechanical Engineering, University of Maribor, Maribor 2000, Slovenia.

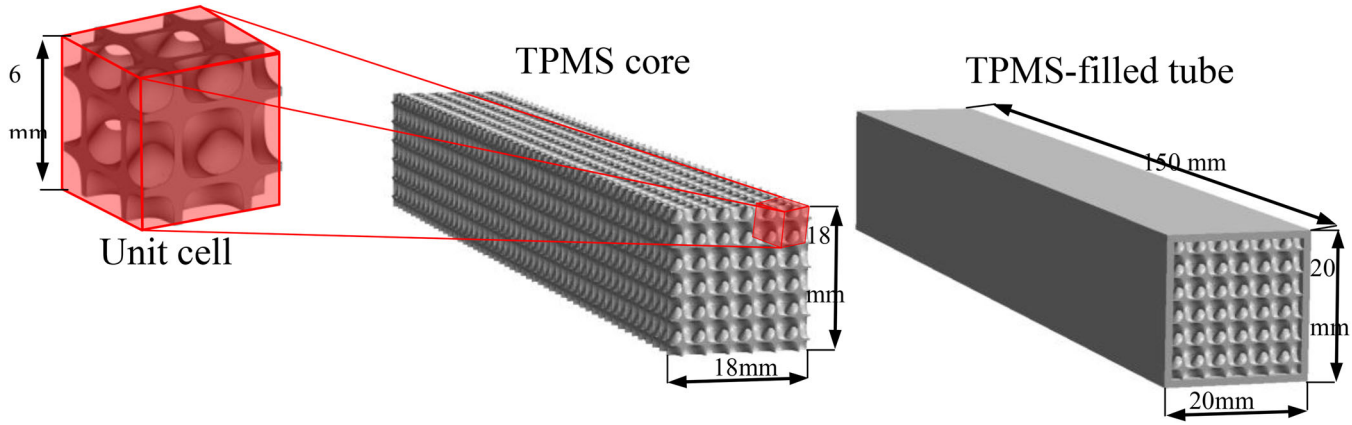

Figure 1. Computer-aided design models of the shell type Diamond foam-filled tubes.

under compression loading conditions [21]. Additionally, the TPMS lattices can be used also as cores for sandwich composites, which results in decreased peak force and increased absorbed energy [22].

The studies of the bending behavior of foam-filled tubes and TPMS cellular structures are gaining increased interest. The bending behavior of gyroid cores fabricated from plastic and reinforced with carbon fiber ribs was analyzed in [23]. Results showed that these structures are among the most effective materials because of their particular geometry. The bending performance of aluminum tubes filled with different cores (APM foam, hybrid APM foam and Metallic Hollow Sphere Structures (MHSS)) was analyzed in recent work [24]. The results show that a reliable and predictable mechanical behavior and failure can be achieved with a proper combination of tubes and cellular metal core with careful material combination and heat treatment. The bending response of carbon fiber reinforced plastic (CFRP) tubes filled with aluminum honeycomb under dynamic impact was evaluated [25]. The specific energy absorption of foam-filled tubes was increased up to 26.8% compared to hollow tubes. The aluminum foam and tube connection were studied under compression and bending loading in [26], where three different joining techniques were evaluated: joining with heat dilatation, pressing and adhesive bonding. The adhesive bonding was found as the most suitable. The foam-filled beams can also successfully enhance the performance of coach structures under rollover conditions, as shown in [27].

Due to the importance of energy-absorbing bending components, it is crucial to study the mechanical behavior of TPMS-filled tubes under bending loading conditions to provide the basis for future real-life applications of these modern composites. Importantly, the role of the interface bonding on the exhibited properties of *ex-situ* and *in-situ* foam-filled tubes is still an open question. In this work, the Diamond TPMS cores, commercially available tubes (hereafter will be referred to as as-fabricated tubes), 3 D printed empty tubes, *ex-situ* and *in-situ* TPMS-filled tubes were tested under bending loading at two different loading velocities. The experimental data was then used to validate the developed computational model, which offers a possibility for developing new graded TPMS-filled tubes with enhanced mechanical properties.

Methods

Geometry and fabrication of specimens

In this work, five different groups of samples were considered. three sets of samples have been fully additively manufactured, namely, (1) the lattice cores, (2) empty tubes, and (3) *in-situ* TPMS-filled tubes. *in-situ* TPMS-filled tubes refer to samples where the tube and the core are fabricated together as one single component (see Figure 1). The other two sets of samples include (4) as-fabricated tubes and (5) *ex-situ* TPMS-filled tubes. *Ex-situ* TPMS-filled tubes are made by inserting the 3 D printed cores inside the commercially available tubes. The lattices were designed and generated using the MSLattice software [28]. the shell type Diamond minimal surface unit cell was chosen for the analysis due to its superior mechanical properties [29]. Lattice cores were designed with 15% relative density and 6 mm unit cell size. Samples were designed with dimensions 20 (18) x 20 (18) x 20 mm and for each group six specimens were fabricated (dimensions given in brackets are for core).

The generated lattice cores, empty tubes and TPMS-filled tubes were fabricated using the powder bed fusion system EOS M280. The additive manufacturing machine uses a 400 W Ytterbium fiber laser with a beam diameter between 100 µm and 500 µm, and scan speeds up to 7 m/s. Gas atomized stainless steel 316 L powder provided by EOSINT (tensile strength 640 ± 50 MPa in XY and 540 ± 55 MPa in Z, and strain at fracture 40 ± 15%in XY and 50 ± 20%in Z) was used to fabricate the plate samples with consistent and repeatable geometry [29]. EOS recommended standard parameters for stainless steel 316 L powders were used. The fabricated samples were blasted with high-pressure air to remove the surrounding residual powder. All the 3 D printed samples were printed vertically such that the long side is in the Z direction. The as-fabricated tubes were made using the high-frequency induction welding from 304-grade stainless steel provided by Marchegaglia company (tensile strength 624 MPa, and strain at fracture 50.6%) and cut to the dimension of the sample using a CNC saw. The wall thickness of as-fabricated tubes was 0.94 mm, while the wall thickness of the 3 D printed tube was 0.98 mm, resulting in a slight weight difference between the two types of empty

Table 1. Dimensions and weight of the samples (st. deviations are shown in brackets).

Dimensions [mm]	18 × 18 × 150	20 × 20 × 150			
Sample	Core	As-fabricated tube	3D printed tube	*Ex-situ* TPMS-filled tube	*In-situ* TPMS filled tube
Weight (st.dev) [g]	58.36 (0.15)	83.75 (0.35)	87.85 (0.18)	142.97 (0.28)	148.23 (0.40)

tubes. The dimensions and weight of fabricated samples are given in Table 1.

Experimental testing

Three-point bending tests under quasi-static and dynamic loading conditions were performed using a servo-hydraulic dynamic testing machine INSTRON 8801 with the position-controlled cross-head rate of 0.25 mm/s (quasi-static) and 284 mm/s (dynamic). The used velocity in quasi-static tests represents a standard velocity (strain rate approx. 0.01 s^{-1}) for testing of similar cellular structures to observe quasi-static loading regime [24], while the velocity in the dynamic tests is the highest possible on the available INSTRON 8801 testing machine. The testing conditions were the same for all samples. All the responses of single samples are presented with the dotted lines, while the average curves are represented with the solid line. To compare the mechanical responses of different samples, the SEA and Crash Force Efficiency (CFE) values were calculated as follows:

$$\mathrm{SEA} = \frac{\int_0^d F(x)dx}{m} \tag{1}$$

and

$$\mathrm{CFE} = \frac{\mathrm{aver}_{\varepsilon<d}\, F}{\mathrm{max}_{\varepsilon<d}\, F} \times 100\%, \tag{2}$$

where d is the displacement at which the values are evaluated, x is displacement, and m is the mass of the sample. The SEA provides the information about the capability of the energy absorption normalized by mass, while the CFE provides the information of uniformity of the force-displacement curve.

The Digital Image Correlation (DIC) was used to evaluate the deformation behavior of samples in quasi-static tests. The images were captured with a SONY HDR-SR8 video camera (2848 × 2136 resolution, 25 frames per second). The GOM Correlate 2019 software was used, where a surface component with facet sizes ~25 pixels, matching against the previous stage, was defined across the sample.

The deformation behavior of samples in dynamic bending tests was also observed with the infrared (IR) thermography. The Flir SC 5000 high-speed cooled middle-wave IR thermal camera (frame rate 608 Hz with 0.02 K sensitive cooled middle-wave InSb detector) was used for IR thermography to observe the evolution of plastic deformation and fracturing of specimens during dynamic compression testing. This approach is suitable for determining crushing deformation patterns in different cellular materials subject to complex loading conditions [2, 27] and proves to be a reliable tool for validating computational models [30].

Table 2. The MAT_024 material model parameters of the base material.

ρ [kg/m^3]	E [MPa]	ν [-]	σ_{yield} [MPa]	σ_2[MPa]	$\varepsilon_{\mathrm{pl},2}$ [-]
7850	210,000	0.3	450	650	0.3

Computational modeling

The MSLattice software was used to generate the mid surfaces that were then used in the computational models and assigned a shell finite element mesh [28], which was done by using the PrePoMax software [31]. The boundary conditions were defined using the LS-PrePost software. The LS-DYNA finite element software [32] was used for all computer simulations presented in this study. The elasto-plastic material model (MAT_024) was used as the base material's constitutive behavior [32]. Inverse computational simulations of loaded samples were used to determine the material parameters to retrieve the same macroscopic simulation results as those measured in experimental testing of all TPMS geometries. The inversely determined material parameters are listed in Table 2. The parameters for the material model MAT 024 are the following: density ρ, Young's modulus E, Poisson's ratio ν, initial yield stress σ_{yield}, linear hardening model with the second point in the stress-strain diagram (σ_2, $\varepsilon_{\mathrm{pl},2}$). The ideal plasticity was assumed after the $\varepsilon_{\mathrm{pl},2}$ to avoid nonphysical removal of finite elements (FE) in the case of considered failure. Inversely determined material parameters for additively manufactured material are similar to those reported for AISI 361 L in [33], where the material parameters were determined using different standard tensile and shear specimens.

The TPMS core was also modeled as a homogenized core to allow for fast and straightforward calculation of the global cellular structure's deformation. The homogenized core was discretized with solid FE with an assigned crushable foam material model (MAT_63). The hardening behavior of the cellular core material model was defined according to the results of quasi-static uniaxial compression testing [29] with Young's modulus of 2 GPa and Poisson's ratio equal to 0. The results of validation and deformation behavior of discrete and homogenized computational are shown in Figure 2.

The supports and the loading cylinder were modeled as linear-elastic (material model MAT_ELASTIC) with the following material parameters: density $\rho = 7850\,\mathrm{kg/m^3}$, Young's modulus $E = 210$ GPa and the Poisson's ratio $\nu = 0.3$.

Finite element mesh and boundary conditions

Fully integrated shell FE with two through-thickness integration points were used to discretize the tube's and discrete TPMS core's geometry, while the fully integrated solid FE were used to model the homogenized core. The mesh sensitivity analysis was performed with three different FE meshes and three different numbers of through-thickness integration

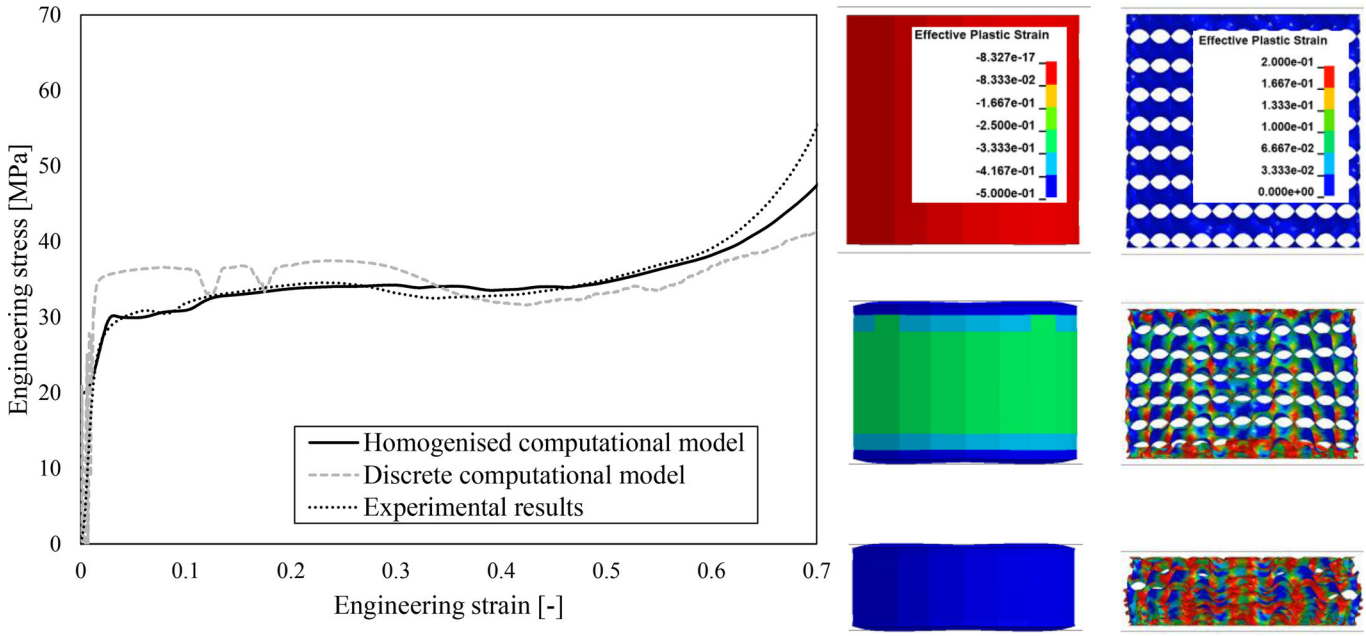

Figure 2. Validation of material models of discrete and homogenized computational models of TPMS cellular structures.

points. The approximate global size of FE was 0.25 mm, which results in approx. 3,760 elements for tube, 6,075 elements for homogenized core and 1,486.925 elements for the discrete core. The mesh convergence study was done for the 3 D printed empty tube, where 8, 10, 12 and 20 elements on the side of the tube (length of side is 20 mm) were analyzed (Figure 4a). The Belytschko-Tsay shell FE with two through-thickness integration points and the thickness of 1 mm was used to model the supports [32]. The average thickness of shell FE in computational models was determined using weight comparison between the CAD model, fabricated specimens (micro-computed tomography), and discretized computational models. The following boundary conditions were used: the bottom supports had all degrees of freedom fixed, the top loading cylinder had prescribed constant velocity in the direction of the negative z-axis (Figure 3). Only one loading velocity was analyzed in computational simulations, the increase from 284 mm/s to 2 m/s was used to speed up the simulations and was confirmed as acceptable by the computational analysis (Figure 4b).

The node to surface contact formulation with friction was defined between tube and supports, while the general contact with friction was defined for self-contact of the TPMS cellular structure. The static and dynamic friction coefficients were set to 0.36 and 0.34, respectively [34]. The node to surface contact was used for the contact between the tube and core, additionally "tied" option was prescribed for in-situ TPMS-filled tubes.

Experimental testing results

TPMS core

The bending behavior of the TPMS diamond core is shown in Figure 5a,b. The DIC analysis results of quasi-static response are shown in Figure 5a), while Figure 5b shows the combined DIC and IR thermography results for the dynamic load case illustrating the classification and fracture development. The mechanical relationship between the loading force and bending displacement is shown in Figure 5c, where a smooth and progressive transition between the linear region and the plastic region. A negligible discrepancy between the sample's behavior can be observed until the first fracture at approximately 20 mm of displacement. A minor strain hardening effect can be observed at displacements larger than 12 mm in the case of dynamic loading. The final deformation of the sample under dynamic loading is shown in Figure 5d, while the cross-section view obtained by longitudinal cut with wire electric discharge cutting of the sample is shown in Figure 5e. The final deformation of the core under quasi-static and dynamic loading is the same.

Computationally, the deformation behavior of the homogenized and discrete core is shown in Figure 6a,b for the dynamic loading case. The mechanical behavior of computational models agrees very well with the experimental results up to 10 mm displacement (Figure 6c). At larger displacements, the local deformation of the discrete core results in stiffness decrease. In contrast, the stiffness decrease is not observed in the homogenized core due to the used material model without failure. The computationally predicted deformation behavior corresponds well to the experimental results, which is also observed in the deformed geometry analysis shown in Figure 6d.

As-fabricated and 3 D printed empty tubes

The mechanical behavior of as-fabricated empty tubes under bending loading is shown in Figure 7a,b. The formation of the plastic zone is generated under the top loading cylinder, which can be seen from IR images. The mechanical responses in Figure 7c show the same elastic response but evident strain-rate hardening in the case of dynamic loading

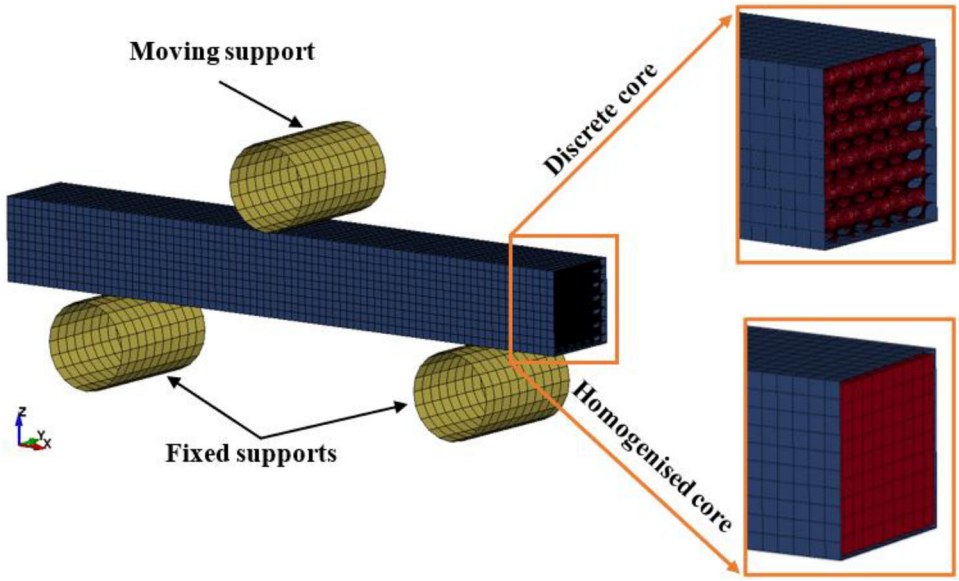

Figure 3. Computational model of TPMS lattice.

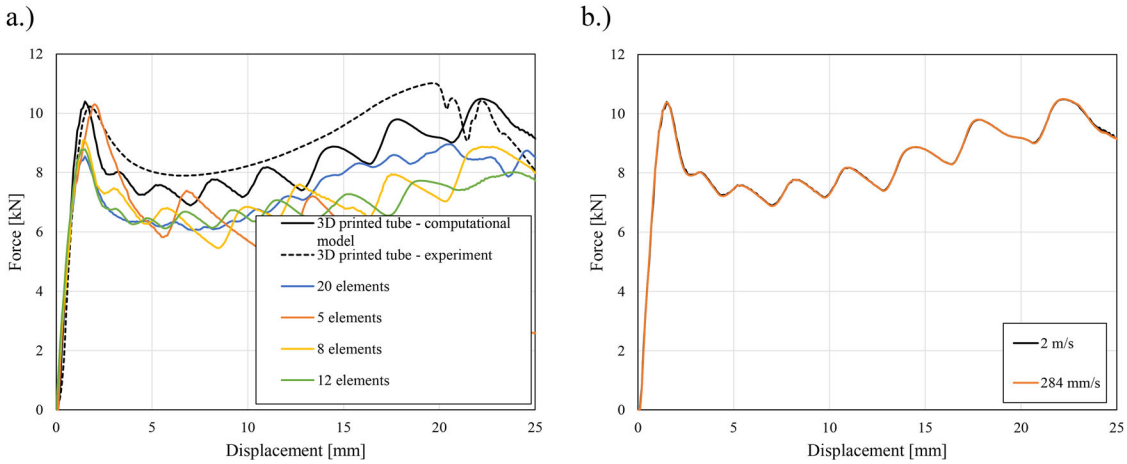

Figure 4. Mesh (a) and loading velocity (b) convergence study.

compared to quasi-static loading. A force drop is observed at about 18 mm displacement in dynamic loading, which is a consequence of the movement (slip) of the tube on the supports. The final deformation of the samples is shown in Figures 7d,e, where Figure 7d corresponds to the dynamic loading, while the cross-section view of the sample after quasi-static loading is shown in Figure 7e. A significant difference in the final deformation can be observed with more localized deformation in dynamic loading which is also the reason for the force drop at larger displacements.

The deformation behavior of 3 D printed empty tubes is shown in Figure 8a,b. The deformation behavior up to moderated displacements is very similar to as-fabricated tubes. The deformation is localized in a smaller area in 3 D printed tubes at larger displacements than in as-fabricated tubes. The peak force of 3 D printed tubes is 16.3% higher compared to as-fabricated ones (see quantitative value in Table 3), while at the same time, similar strain-rate hardening is observed. In dynamic loading, the force increases at displacements above 13 mm, while the it decreases in the quasi-static loading case at the same displacement. The final deformation of the sample under dynamic loading is shown in Figure 8d, while the cross-section view of the sample after quasi-static loading is shown in Figure 8e. There is a clear difference in the final deformation in the case of quasi-static and dynamic loading. The deformation is more localized in the case of quasi-static loading, which caused the stiffness drop. Compared to the as-fabricated empty tubes, the 3 D printed tubes exhibit more localized deformation in the case of quasi-static loading, leading to stiffness decrease at displacements above 13 mm.

Figure 9a,b present the results of the numerical simulations for the as-fabricated and 3 D printed tubes. The mechanical behavior of the computational model corresponds well with the experimental results in terms of peak force (Figure 9c). However, a higher drop after the peak force is observed in the computational model compared to the experimental response, especially in as-fabricated tubes. Similar to the experimental results, the force drops until 13 mm displacement after the first peak after which it starts to increase again. The SEA obtained by the computational results is approximately 10% lower than the values obtained experimentally. The final deformation of the as-fabricated

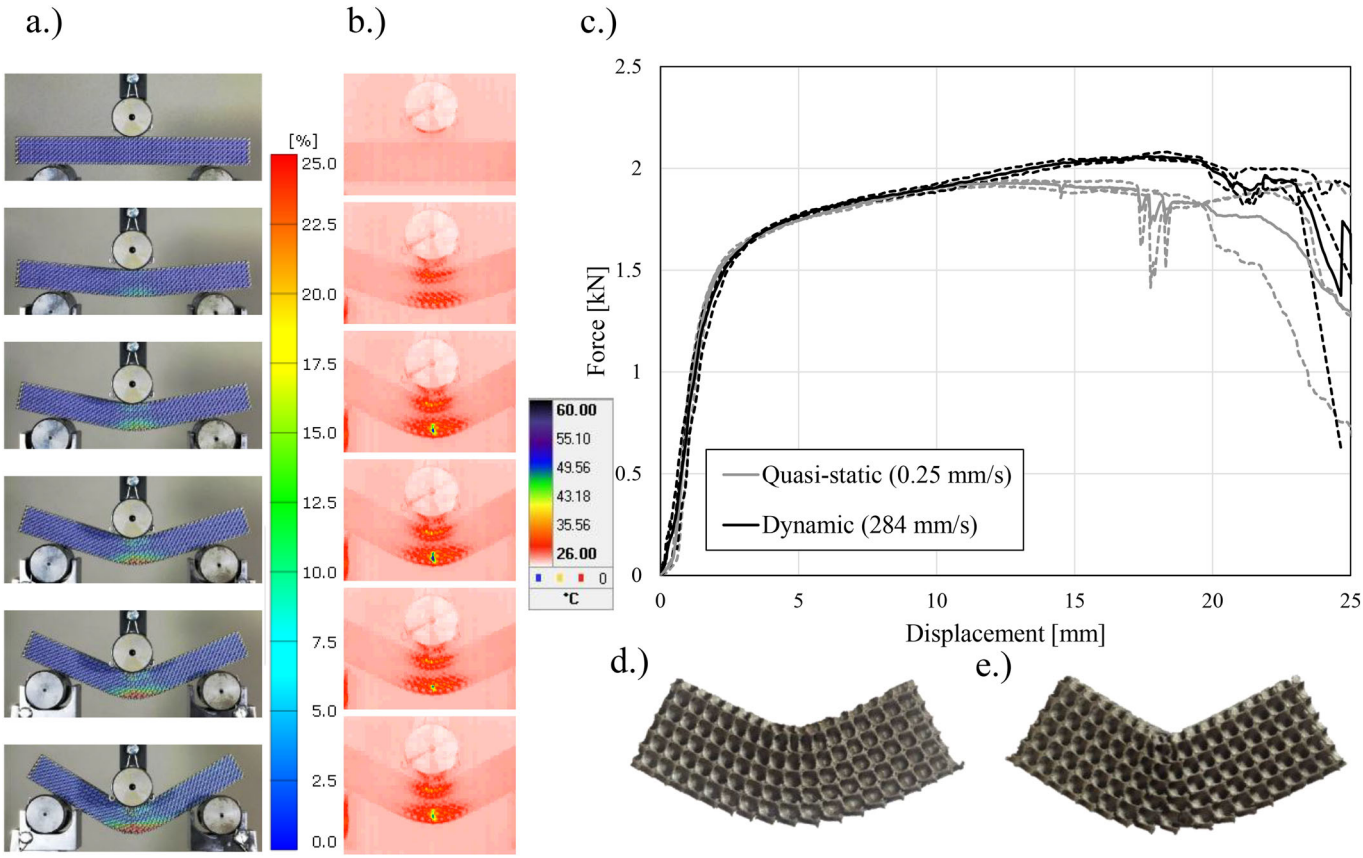

Figure 5. Deformation and mechanical behavior of 3 D printed core. a) quasi-static testing and DIC, b) dynamic testing and IR thermography, c) mechanical response, d) deformed sample, and e) a cross-section of the deformed sample.

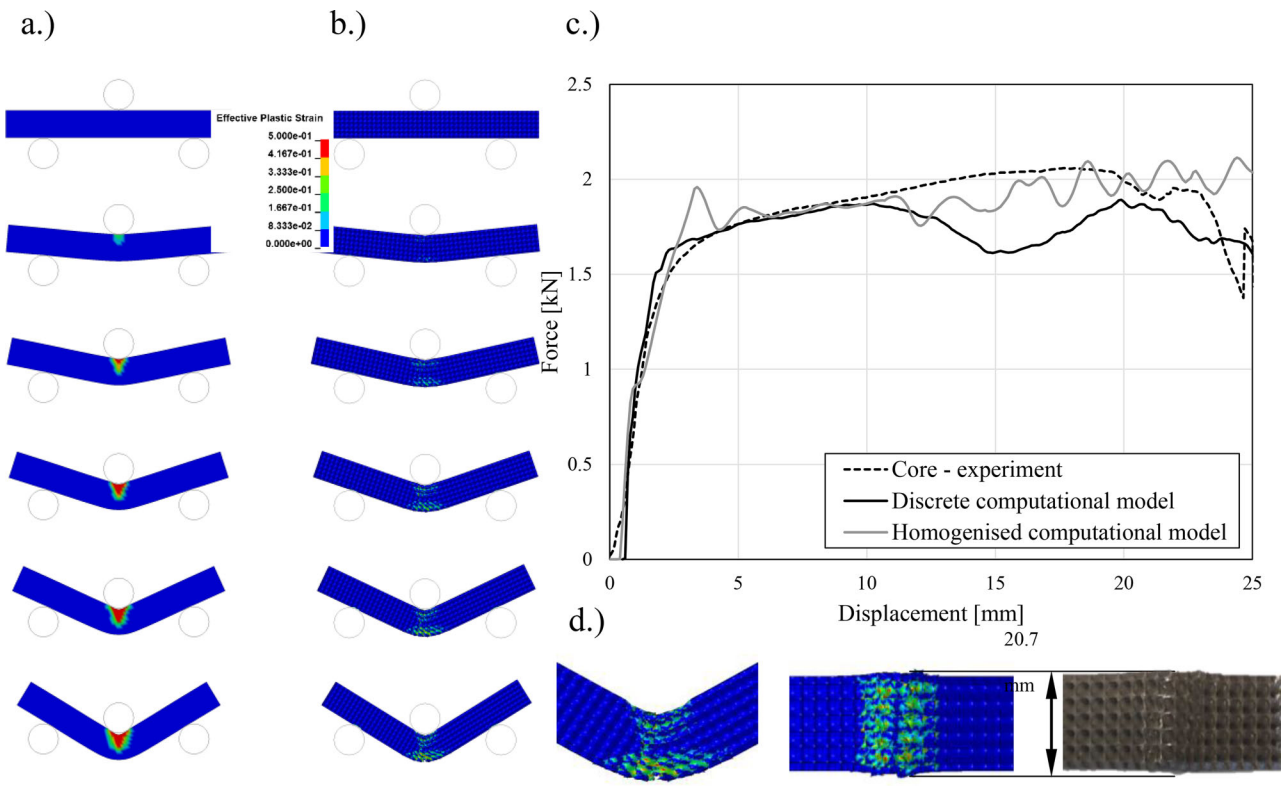

Figure 6. Deformation and mechanical behavior of a homogenized and discrete computational model of core in case of dynamic loading (displacement step 5 mm). a) Deformation behavior of homogenized core, b) deformation behavior discrete core, c) comparison to experimental results, and d) comparison of final deformation.

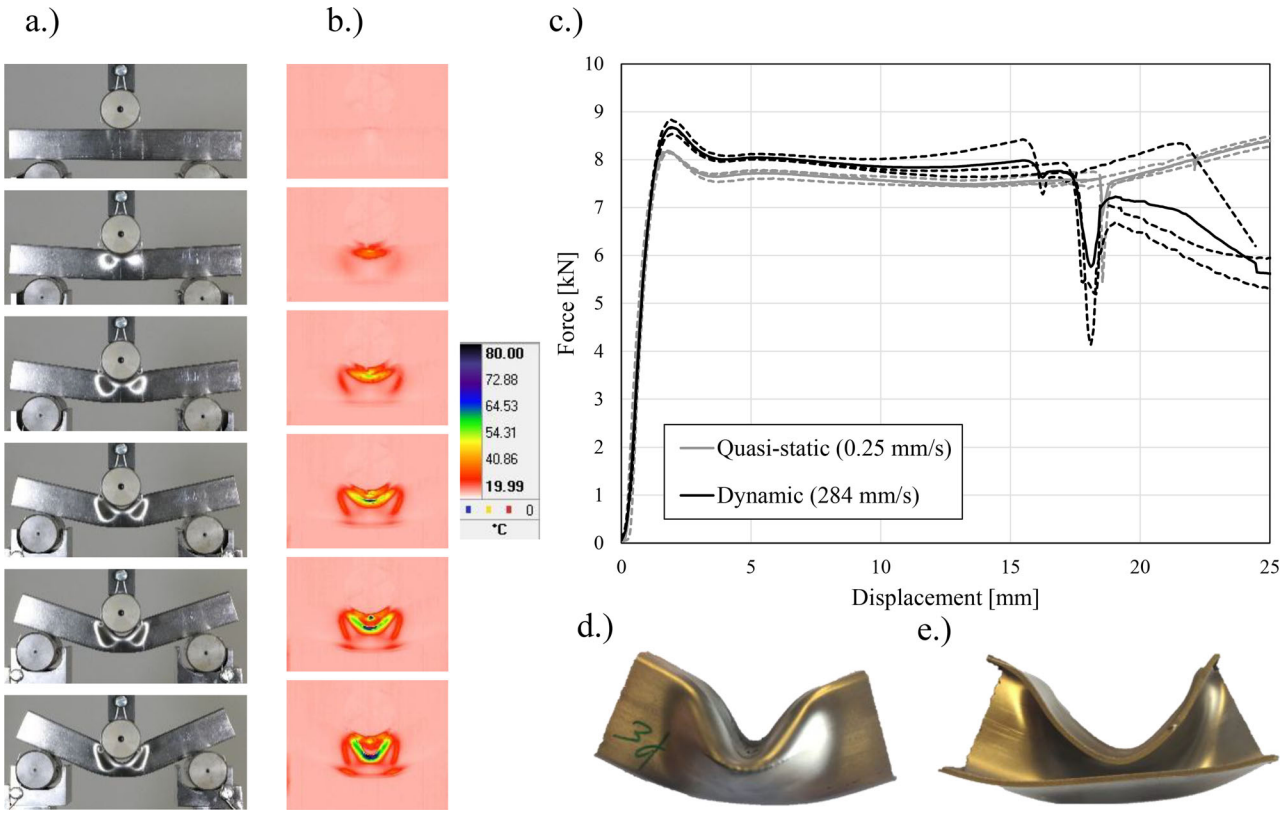

Figure 7. Deformation and mechanical behavior of as-fabricated tubes. a) Quasi-static testing, b) dynamic testing and IR thermography, c) mechanical response, d) deformed sample and e) a cross-section of the deformed sample.

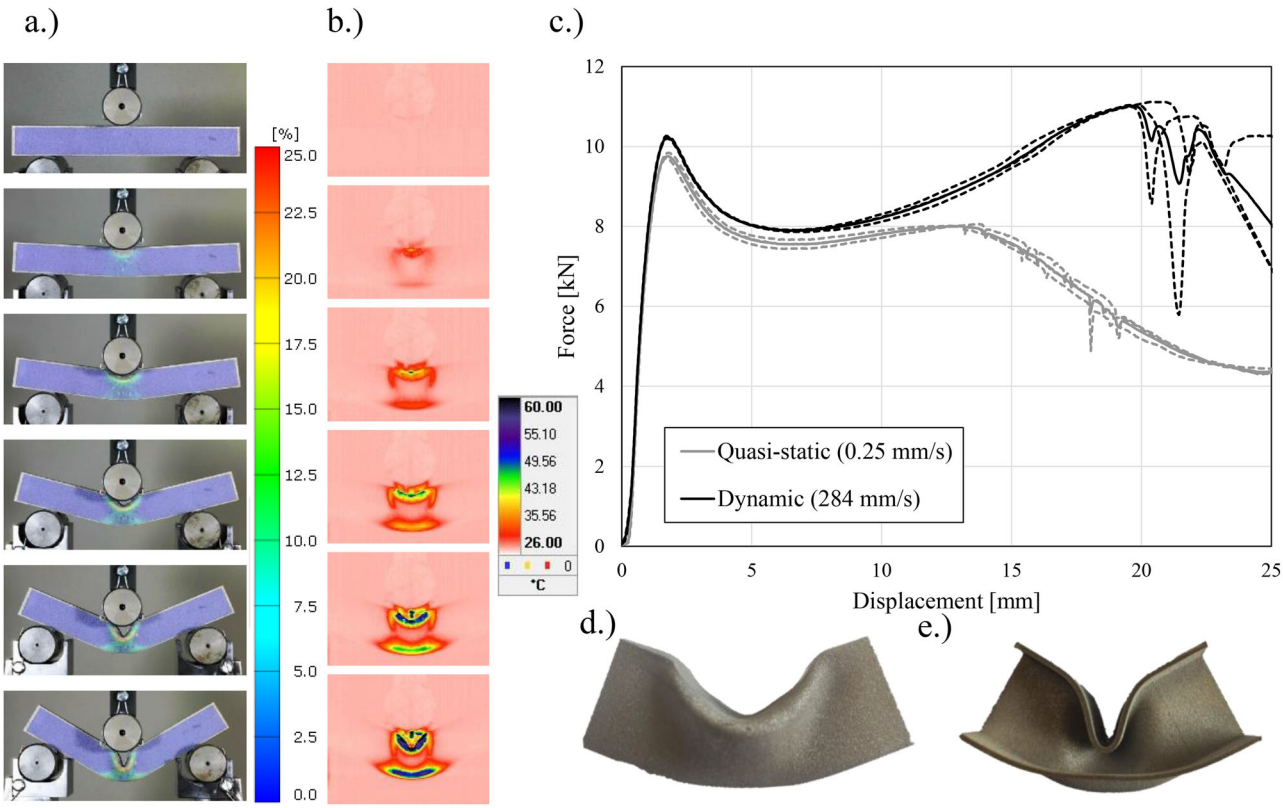

Figure 8. Deformation and mechanical behavior of 3 D printed tubes. a) Quasi-static testing and DIC, b) dynamic testing and IR thermography, c) mechanical response, d) deformed sample and e) a cross-section of the deformed sample.

Table 3. Experimental values of peak force and SEA results of bending testing.

	Peak force [kN] (displacement [mm])		SEA [J/g]					
			@10 mm		@15 mm		@20 mm	
Sample	QS	DYN	QS	DYN	QS	DYN	QS	DYN
Core	1.93 (12.9)	2.06 (17.7)	0.27	0.27	0.43	0.44	0.59	0.61
As-fabricated tube	8.17 (1.8)	8.67 (1.9)	0.86	0.90	1.31	1.37	1.76	1.81
3D printed tube	9.76 (1.8)	10.23 (1.8)	0.86	0.90	1.31	1.40	1.68	2.00
Ex-situ TPMS-filled tube	16.57 (13.3)	18.77 (13.2)	0.92	0.98	1.50	1.59	2.06	2.19
In-situ TPMS-filled tube	15.95 (10.5)	17.99 (17.6)	0.93	0.97	1.46	1.57	1.96	2.71

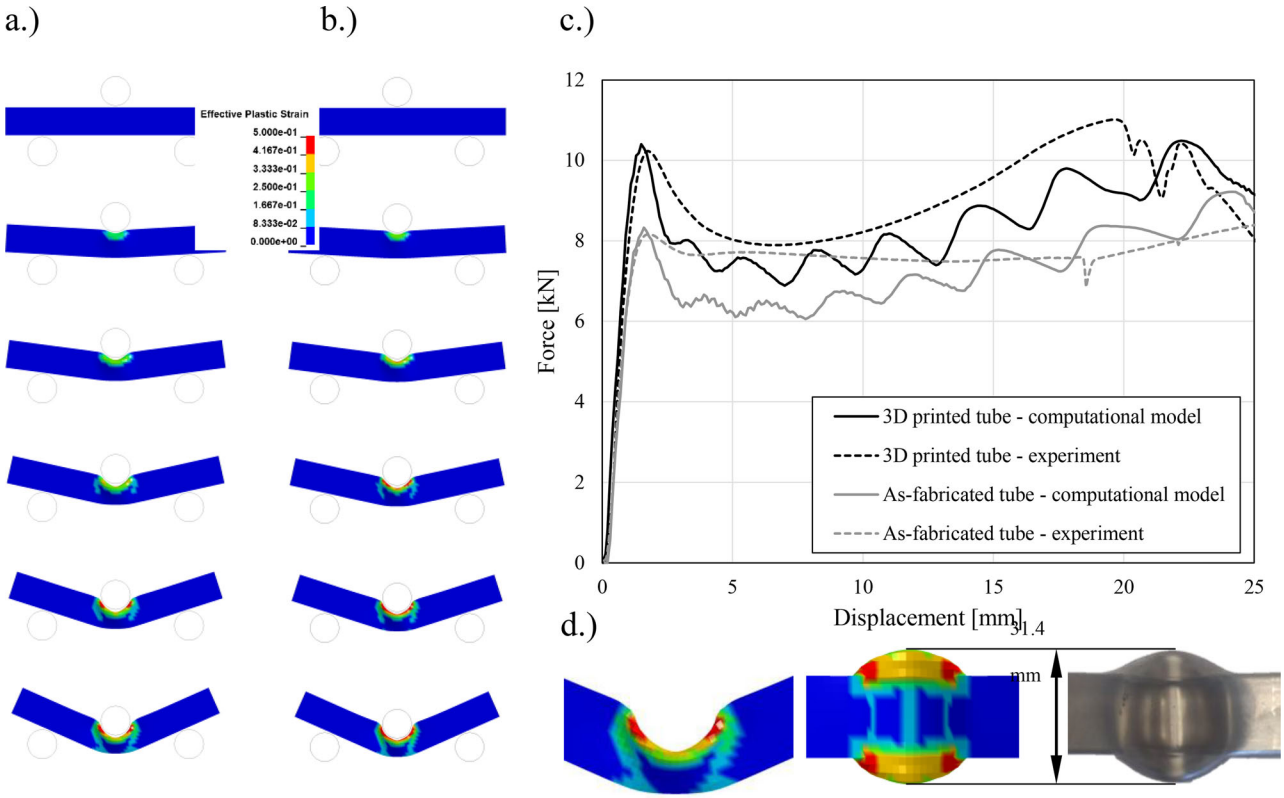

Figure 9. Deformation and mechanical behavior of as-fabricated and 3 D printed tube's computational model in case of dynamic loading. a) Deformation behavior of as-fabricated tube, b) deformation behavior of 3 D printed tube, c) comparison to experimental results, and d) final deformation comparison.

tubes is shown in Figure 9d. The computationally predicted final deformation corresponds very well to the experimental observations.

In-situ and ex-situ TPMS filled tubes

The bending behavior of *in-situ* TPMS filled tubes is shown in Figure 10a,b. The deformation is localized at the top and bottom side of the tube, while the middle part around the neutral axis is not deformed. The shape of the force-displacement response is more influenced by the response of the core rather than the empty tube. The drop in force after the first peak that was observed in the case of empty tubes is eradicated by the presence of the lattice core and a more progressive response is obtained. Strain rate hardening is observed where again the hardening is observed in the case of dynamic loading and softening in the case of quasi-static loading, same as in the case of 3 D printed empty tubes. The final deformation of the sample under dynamic loading is shown in Figure 10d, while the cross-section view of the sample after quasi-static loading is shown in Figure 10e. There is a minor difference in the final deformation in the case of quasi-static and dynamic loading. The deformation is slightly more localized in quasi-static loading, which results in the force drop after reaching the maximum loading force at around 11 mm. As shown in Figure 10e, the core is deformed locally in the area of the top-loading cylinder.

The bending behavior of *ex-situ* TPMS filled tubes is shown in Figure 11a,b, where it can be observed that the deformation behavior is very similar to the *in-situ* TPMS filled tubes. The core fits very well in the tube, and the slip out from the tube is minimal. The mechanical response shown in Figure 11c reveals that the *ex-situ* TPMS filled tube slips at the supports at certain displacement in case of dynamic loading. This results in the force drop and further stiffness decrease, same as in empty as-fabricated tubes. The final deformation of the sample under dynamic loading is shown in Figure 11d, while the cross-section view of the sample after quasi-static loading is shown in Figure 11e.

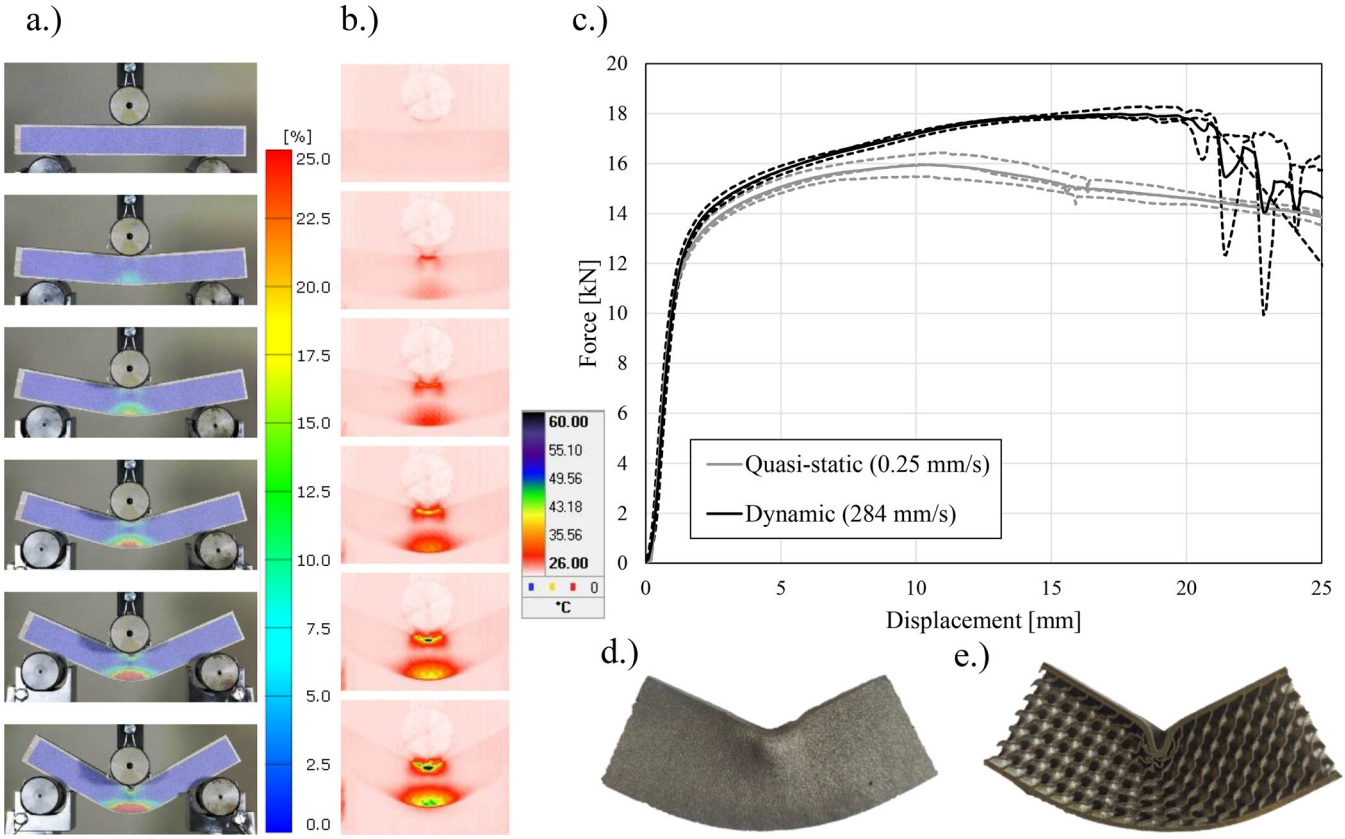

Figure 10. Deformation and mechanical behavior of *in-situ* TPMS-filled tube. a) Quasi-static testing and DIC, b) dynamic testing and IR thermography, c) mechanical response, d) deformed sample and e) a cross-section of the deformed sample.

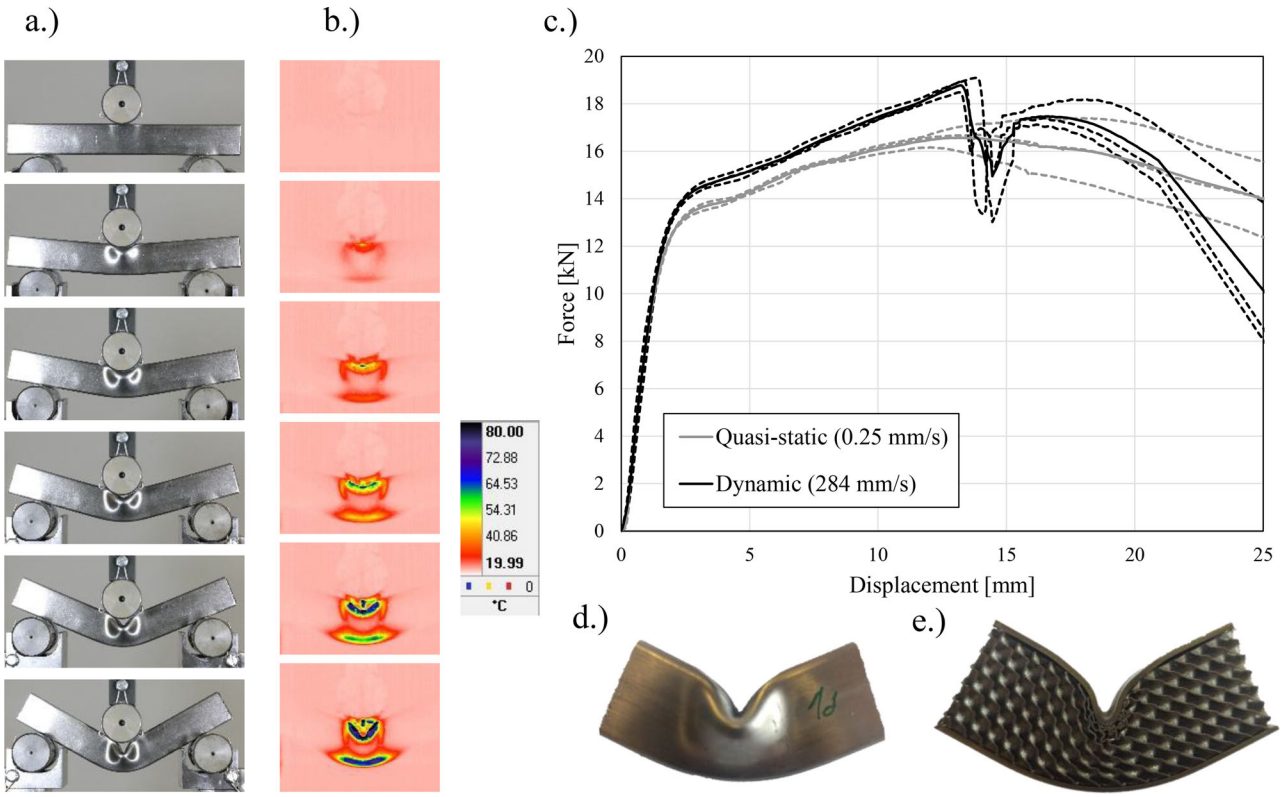

Figure 11. Deformation and mechanical behavior of *ex-situ* TPMS-filled tubes (a – quasi-static testing, b – dynamic testing and IR thermography, c – mechanical response, d – deformed sample and e – a cross-section of the deformed sample).

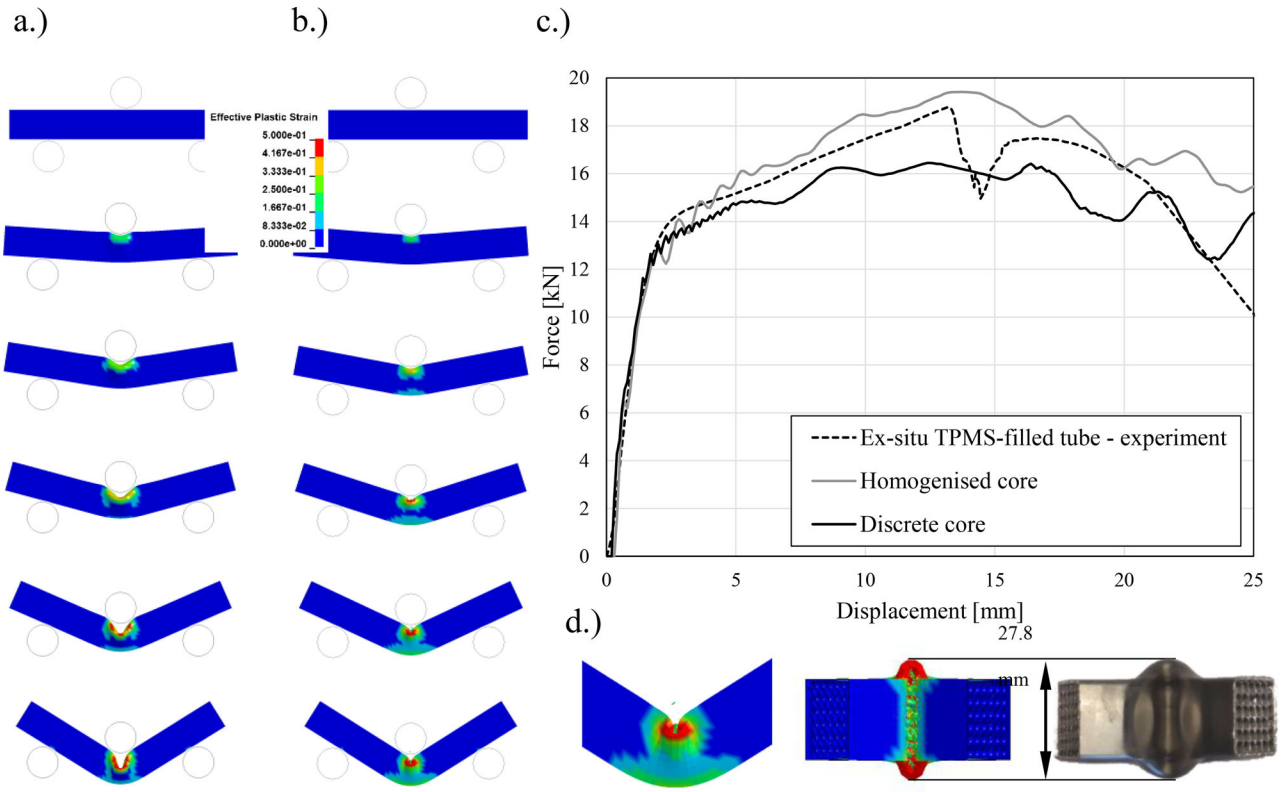

Figure 12. Deformation and mechanical behavior of *ex-situ* TPMS-filled tubes computational model in case of dynamic loading (a – deformation behavior of the computational model with homogenized core, b – deformation behavior of the computational model with discrete core, c – comparison to experimental results, d – final deformation comparison).

There is no difference in the final deformation between quasi-static and dynamic loading cases. The mechanical responses are very similar up to large displacement if neglecting the force drop caused by tube slipping at the supports in dynamic loading. The slipping is much slower and stable in the case of quasi-static loading. The ex-situ TPMS filled tubes are deformed locally in the area of the top-loading cylinder (Figure 11e), similar to the *in-situ* TPMS-filled tubes (Figure 10e).

Computationally, the same material model of tubes and core was also used in the simulations of TPMS-filled tubes. A good correlation between the computational and experimental results can be observed in *ex-situ* TPMS filled tubes. Some discrepancy of results at larger displacements is observed in *in-situ* TPMS-filled tubes for both discrete and homogenized computational models (Figures 12 and 13). The discrepancy is a consequence of the tie contact between the tube and core, where the core elements tied to the tube fail, causing a slight movement of the core inside the tube, which results in decreased stiffness. The final deformation is more localized in the case of the computational model (Figures 12d and 13d).

Results comparison

A qualitative comparison of the quasi-static bending mechanical responses is shown in Figure 14. The comparison of as-fabricated and 3 D printed tubes shows a higher initial peak in the 3 D printed tubes, which is in part a consequence of a 5% larger weight of 3 D printed tubes (Table 1). However, it should be noted also that the mechanical properties of 3 D printed tubes are direction-dependent and part of the difference in mechanical properties between the as fabricated and the 3 D printed tubes can be attributed to the difference in properties between the base materials despite the fact that the reported properties of the base materials are fairly comparable. After the first peak, 3 D printed tubes' force decreases at displacements larger than 13 mm, which is not the case in as-fabricated tubes. The results of foam-filled tubes showed that the *ex-situ* and *in-situ* TPMS-filled tubes provide very similar responses, with a slightly stiffer elastic response of *in-situ* TPMS-filled tubes due to a better interface connection between the core and the tube. The effect of interface interaction can be observed in Figure 14, where the responses of empty tubes and core are summed and they show up to 41% lower peak force compared to *ex-situ* TPMS-filled tubes and 31% lower peak force compared to *in-situ* TPMS-filled tubes.

Quantitative results of mechanical responses are given in Table 3. In general, peak forces in dynamic loading appear at larger displacements and are about 6% (core and empty tubes) and 13% (ex-situ and in-situ) higher than those achieved in quasi-static testing. The second peak in the dynamic loading of the 3 D printed tube (11.01 kN at the displacement of 19.7 mm) was neglected for that analysis. The peak forces of the foam-filled tubes are 65%–80% larger than the sum of the core and empty tubes. The values of SEA were compared at the displacements of 10 mm, 15 mm and 20 mm. Similar to peak forces, the strain rate hardening is more pronounced in the case of *ex-situ* and *in-situ* TPMS-filled tubes. The *in-situ* TPMS filled tubes provide

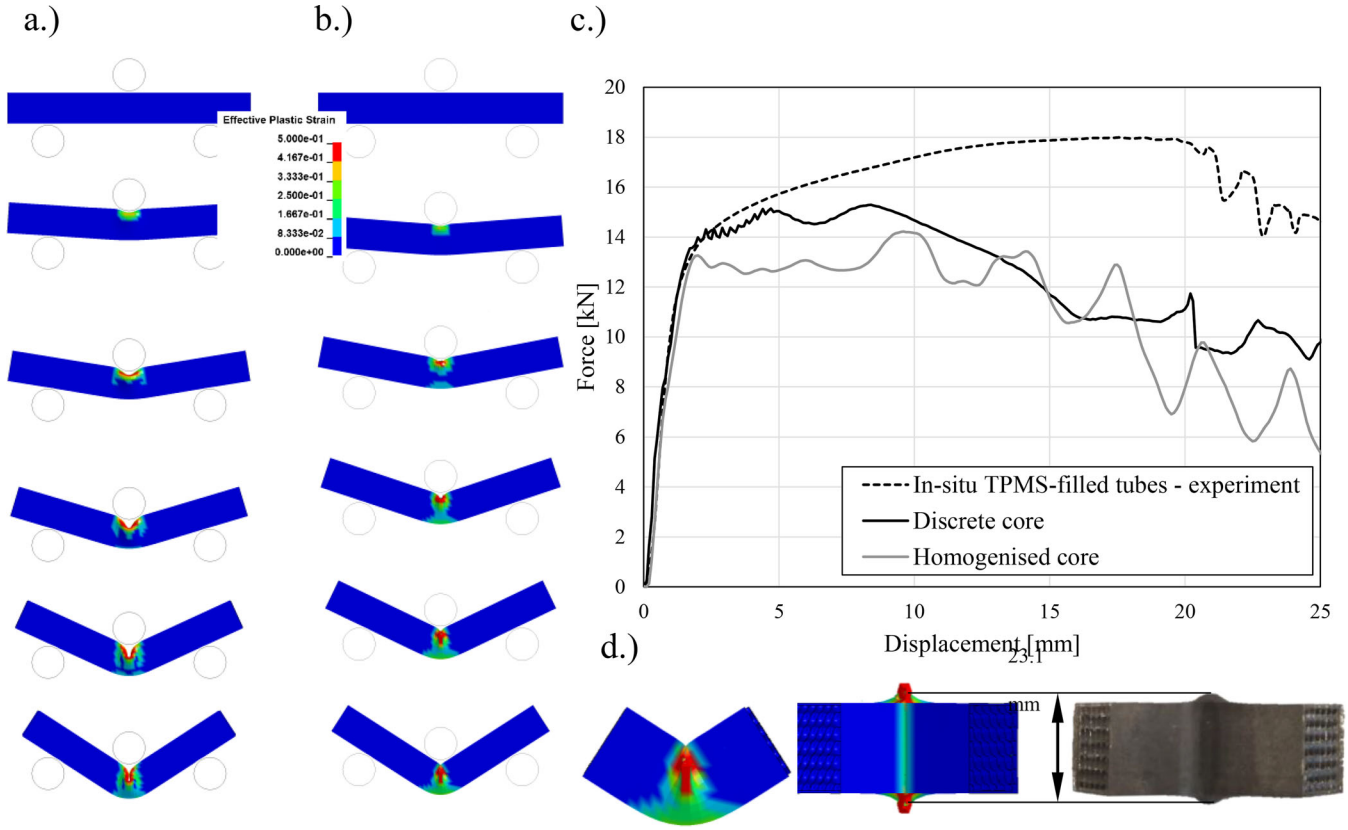

Figure 13. Deformation and mechanical behavior of *in-situ* TPMS-filled tubes computational model in case of dynamic loading (a – deformation behavior of the computational model with homogenized core, b – deformation behavior of the computational model with discrete core, c – comparison to experimental results, d – final deformation comparison).

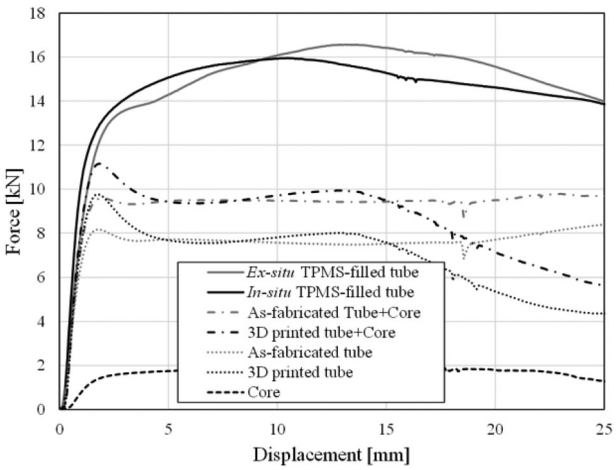

Figure 14. Comparison of the force-displacement responses of the different samples.

higher SEA at displacements up to 10 mm, while the *ex-situ* TPMS filled tubes provide slightly higher values of SEA at displacements larger than 10 mm. The SEA at 20 mm displacement is increased up to 40% in *ex-situ* TPMS-filled tubes and up to 46% in *in-situ* TPMS-filled tubes compared to the summed responses of core and empty tubes.

The CFE values are given in Table 4 and are provided for displacements, at which peak forces of all samples are reached (unless for the core, but the peak force at 15 mm is 1% lower than overall peak force). At a displacement of 15 mm, as-fabricated tubes and TPMS-filled tubes provide

Table 4. Experimental values of CFE of bending testing.

	CFE [%]			
	@15 mm		@20 mm	
Sample	QS	DYN	QS	DYN
Core	85.04	81.97	87.84	85.34
As-fabricated tube	87.69	86.18	88.84	85.78
3D printed tube	76.88	78.65	74.22	78.49
Ex-situ TPMS-filled tube	86.24	80.90	88.81	83.37
In-situ TPMS-filled tube	88.39	84.80	89.64	88.06

comparable and much higher values than reported in the literature [35]. In general, CFE values are lower in the case of dynamic loading, which is mainly caused by the higher peak forces compared to the quasi-static loading. The values of CFE at 20 mm increased and showed superior behavior of *ex-situ* and *in-situ* TPMS-filled tubes, reaching CFE of 90%. The high value of CFE is indicator of uniformity of the mechanical response (force-displacement curve), which can be very beneficial in energy absorbing applications.

We extended the study using the validated discrete computational model to investigate *ex-situ* TPMS-filled tubes with different uniform and graded relative densities (RD). The peak force and SEA values were computationally obtained for uniform cores with 12% and 18% RD and were compared to the initial core with 15% RD. The effect of a graded core was considered next, with a lower RD of 9% in the inner part of the core and a higher RD of 15% in the outer part (Figure 15a). The graded core had an overall relative density of 13%.

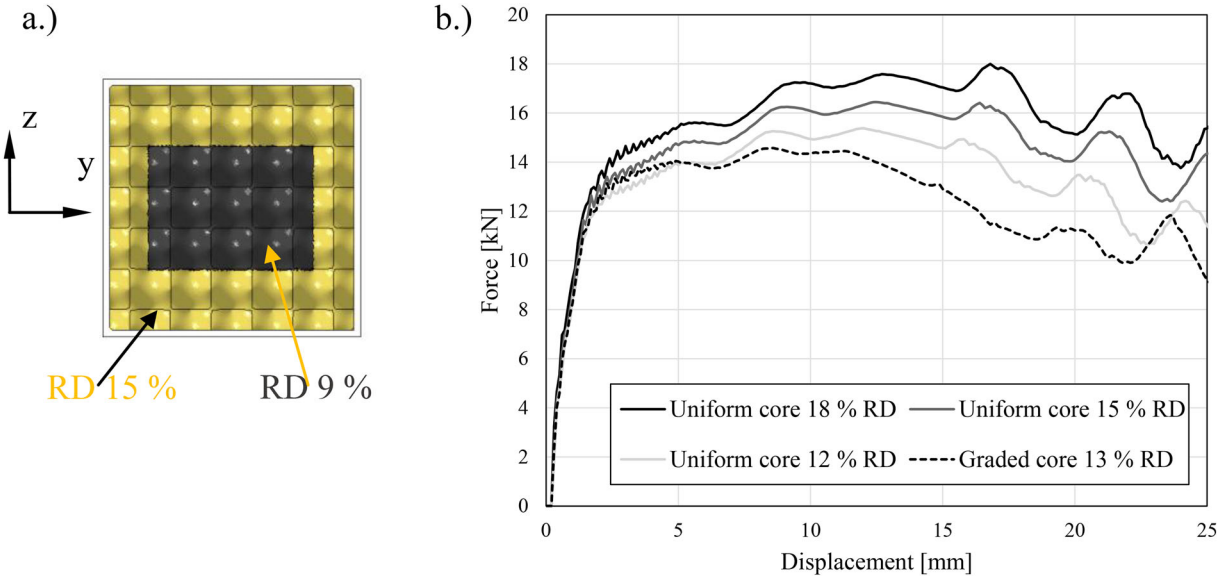

Figure 15. Cross-section of graded core (a) and mechanical responses of cores with different RD and graded core (b).

Table 5. Peak force and SEA analysis for the different relative density cores.

		SEA [J/g]		
Sample	Peak force [kN] (displacement [mm])	@10 mm	@15 mm	@20 mm
Uniform core RD 18 %	18.00 (16.92)	0.91	1.47	2.01
Uniform core RD 15 %	16.45 (12.54)	0.95	1.51	2.05
Uniform core RD 12 %	15.38 (12.01)	0.98	1.56	2.08
Graded core RD 13 %	14.58 (8.26)	0.95	1.46	1.90

The mechanical responses of the uniform and graded cores with different relative densities are shown in Figure 15b. These responses exhibited a very similar mechanical response while differing only in peak forces corresponding to different relative densities of the samples.

The peak forces and the values of SEA are listed in Table 5. As expected, the core with the highest RD provides the highest peak force. The uniform core with the lowest RD provides the highest SEA, which signifies that the stiffness ratio between the tube and core can be optimized. The graded core provides the lowest peak force but provides the second-highest SEA up to 10 mm displacement simultaneously, which can be beneficial in many applications.

Conclusions

The bending behavior of TPMS-filled tubes under two different loading velocities was evaluated in this study. The TPMS core, empty as-fabricated and 3 D printed tubes were mechanically tested first. The tests showed that the first response peak is higher in 3 D printed tubes, while the overall mechanical behavior is very similar to the as-fabricated tubes. The *ex-situ* and *in-situ* TPMS-filled tubes were then tested. While the *in-situ* TPMS-filled tubes showed to have slightly higher stiffness compared to the *ex-situ* TPMS-filled tubes due to the strong interfacial bond between the core and the tube, no significant difference in terms of energy absorption was observed. The specific energy absorption of TPMS-filled tubes is increased up to 40% in *ex-situ* TPMS-filled tubes and up to 46% in *in-situ* TPMS-filled tubes if compared to the summed responses of core and empty tubes. The highest values of crash force efficiency is also achieved in the case of *in-situ* TPMS-filled tubes and reaches 90%. This showed, that the response of the *in-situ* TPMS-filled tubes is uniform and that these tubes can be superior candidates for future crash-absorbing components.

The computational models of TPMS-filled tubes were developed and validated against experimental results. Two different computational models of core were considered – homogenized and discrete. The discrete computational model enables precise modeling of the TPMS structure deformation behavior and a more straightforward introduction of new graded geometries at the expense of longer computational times. The homogenized computational model provides faster calculation of the TPMS-filled tube's global crushing behavior, which is in most cases enough for predictions of foam-filled tube's behavior in structural engineering designs. The study was computationally extended to investigate uniform and graded core of *ex-situ* TPMS-filled tubes using the validated numerical models. The study results show that the mechanical response of TPMS-filled tubes can be easily adapted using different relative densities or/and distributions of relative density (grading) of the core. Therefore, validated computational models will be used to

develop future graded TPMS-filled tubes with enhanced mechanical properties adapted to the specific application needs.

Acknowledgment

This research was partially carried out using the Core Technology Platforms resources at New York University Abu Dhabi.

Disclosure and declaration of interest statement

The authors report there are no competing interests to declare. The authors declare that there is no conflict of interest connected with the article.

Funding

The authors acknowledge the financial support from the Slovenian Research Agency (fundamental postdoctoral research project (No. Z2-2648) and national research programme funding (No. P2-0063)).

References

[1] H. Zhou, R. Liu, Y. Hu, P. Song, and R. Guo, Quasi-static compressive strength of polymethacrylimide foam-filled square carbon fiber reinforced composite honeycombs, J Sandwich Struct. Mater., vol. 23, no. 6, pp. 2358–2374, 2021. DOI: 10.1177/1099636220909819.

[2] I. Duarte, L. Krstulović-Opara, and M. Vesenjak, Characterisation of aluminium alloy tubes filled with aluminium alloy integral-skin foam under axial compressive loads, Compos. Struct., vol. 121, pp. 154–162, 2015. DOI: 10.1016/j.compstruct.2014.11.003.

[3] I. Duarte, M. Vesenjak, L. Krstulović-Opara, and Z. Ren, Static and dynamic axial crush performance of in-situ foam-filled tubes, Compos. Struct., vol. 124, pp. 128–139, 2015. DOI: 10.1016/j.compstruct.2015.01.014.

[4] A. Kemény, B. Leveles, D. B. Kincses, and D. Károly, Manufacturing and Investigation of in-situ and ex-situ produced aluminum matrix foam-filled tubes, Adv. Eng. Mater., vol. 2100365, pp. 1–8, 2021.

[5] I. Duarte, M. Vesenjak, L. Krstulović-Opara, and Z. Ren, Compressive performance evaluation of APM (advanced pore morphology) foam filled tubes, Compos. Struct., vol. 134, pp. 409–420, 2015. DOI: 10.1016/j.compstruct.2015.08.097.

[6] I. Duarte, L. Krstulović-opara, J. Dias-de-Oliveira, and M. Vesenjak, Axial crush performance of polymer-aluminium alloy hybrid foam filled tubes, Thin Walled Struct., vol. 138, pp. 124–136, 2019. DOI: 10.1016/j.tws.2019.01.040.

[7] X. Yang, et al., The effect of outer tube on quasi-static compression behavior of aluminum foam-filled tubes, Compos. Struct., vol. 245, pp. 112357, Aug. 2020. DOI: 10.1016/j.compstruct.2020.112357.

[8] A. Najibi, P. Ghazifard, and P. Alizadeh, Numerical crashworthiness analysis of a novel functionally graded foam-filled tube, J. Sandwich Struct. Mater., vol. 23, no. 5, pp. 1635–1661, 2021. DOI: 10.1177/1099636219900334.

[9] J. Song, S. Xu, L. Xu, J. Zhou, and M. Zou, Experimental study on the crashworthiness of bio-inspired aluminum foam-filled tubes under axial compression loading, Thin-Walled Struct., vol. 155, pp. 106937, Oct. 2020. DOI: 10.1016/j.tws.2020.106937.

[10] S. Mohsenizadeh, R. Alipour, M. Shokri Rad, A. Farokhi Nejad, and Z. Ahmad, Crashworthiness assessment of auxetic foam-filled tube under quasi-static axial loading, Mater. Des., vol. 88, pp. 258–268, Dec. 2015. DOI: 10.1016/j.matdes.2015.08.152.

[11] S. Mohsenizadeh, and Z. Ahmad, Auxeticity effect on crushing characteristics of auxetic foam-filled square tubes under axial loading, Thin-Walled Struct., vol. 145, no. July, pp. 106379, 2019. DOI: 10.1016/j.tws.2019.106379.

[12] O. Al-Ketan, R. Rowshan, and R. K. Abu Al-Rub, Topology-mechanical property relationship of 3D printed strut, skeletal, and sheet based periodic metallic cellular materials, Addit. Manuf., vol. 19, pp. 167–183, 2018.

[13] D. W. Abueidda, M. Bakir, R. K. Abu Al-Rub, J. S. Bergström, N. A. Sobh, and I. Jasiuk, Mechanical properties of 3D printed polymeric cellular materials with triply periodic minimal surface architectures, Mater. Des., vol. 122, pp. 255–267, 2017. DOI: 10.1016/j.matdes.2017.03.018.

[14] A. Alhammadi, K. A. Khan, O. Al-Ketan, M. I. H. Ali, R. Rowshan, and R. K. Abu Al-Rub, Microstructural Characterization and Thermomechanical Behavior of Additively Manufactured AlSi10Mg Material and Architected Cellular Structures, In: TMS 2020 149th Annual Meeting & Exhibition Supplemental Proceedings. The Minerals, Metals & Materials Series. Springer, Cham, 2020. https://doi.org/10.1007/978-3-030-36296-6_15

[15] D. W. Abueidda, R. K. Abu Al-Rub, A. S. Dalaq, D.-W. Lee, K. A. Khan, and I. Jasiuk, Effective conductivities and elastic moduli of novel foams with triply periodic minimal surfaces, Mech. Mater., vol. 95, pp. 102–115, 2016. DOI: 10.1016/j.mechmat.2016.01.004.

[16] O. Al-Ketan, and R. K. Abu Al-Rub, Multifunctional mechanical metamaterials based on triply periodic minimal surface lattices, Adv. Eng. Mater., vol. 21, no. 10, pp. 1900524, 2019. DOI: 10.1002/adem.20[Mismatch[Mismatch.

[17] O. Al-Ketan, R. Rowshan, A. N. Palazotto, and R. K. Abu Al-Rub, On mechanical properties of cellular steel solids with shell-like periodic architectures fabricated by selective laser sintering, J. Eng. Mater. Technol., vol. 141, no. 2, pp. 1–12, 2019.

[18] A. Alhammadi, O. Al-Ketan, K. A. Khan, M. Ali, R. Rowshan, and R. K. Abu Al-Rub, Microstructural characterization and thermomechanical behavior of additively manufactured AlSi10Mg sheet cellular materials, Mater. Sci. Eng. A., vol. 791, no. February, pp. 139714, 2020. DOI: 10.1016/j.msea.2020.139714.

[19] O. Al-Ketan, D.-W. D.-W. Lee, R. Rowshan, and R. K. R. K. Abu Al-Rub, Functionally graded and multi-morphology sheet TPMS lattices: Design, manufacturing, and mechanical properties, J. Mech. Behav. Biomed. Mater., vol. 102, pp. 103520, 2020.

[20] I. Maskery, and I. A. Ashcroft, The deformation and elastic anisotropy of a new gyroid-based honeycomb made by laser sintering, Addit. Manuf., vol. 36, no. August, pp. 101548, 2020.

[21] H. Yin, D. Tan, G. Wen, W. Tian, and Q. Wu, Crashworthiness analysis and optimization design of TPMS-filled structure, Int. J. Crashworthiness, pp. 1–18, 2021. DOI: 10.1080/13588265.2021.1959171.

[22] O. Fashanu, et al., Mechanical performance of sandwich composites with additively manufactured triply periodic minimal surface cellular structured core, J. Sandw. Struct. Mater., vol. 24, no. 2, pp. 1133–1151, 2021.

[23] M. Pelanconi, and A. Ortona, Nature-inspired, ultra-lightweight structures with gyroid cores produced by additive manufacturing and reinforced by unidirectional carbon fiber ribs, Materials (Basel)., vol. 12, no. 24, pp. 4134–4114, 2019. DOI: 10.3390/ma12244134.

[24] M. Vesenjak, I. Duarte, J. Baumeister, H. Göhler, L. Krstulović-Opara, and Z. Ren, Bending performance evaluation of aluminium alloy tubes filled with different cellular metal cores, Compos. Struct., vol. 234, pp. 111748, 2020. DOI: 10.1016/j.compstruct.2019.111748.

[25] Y. Xiao, Y. Hu, J. Zhang, C. Song, Z. Liu, and J. Yu, Dynamic bending responses of CFRP thin-walled square beams filled with aluminum honeycomb, Thin-Walled Struct., vol. 132, pp. 494–503, Nov. 2018. DOI: 10.1016/j.tws.2018.09.023.

[26] F. Garai, G. Béres, and Z. Weltsch, Development of tubes filled with aluminium foams for lightweight vehicle manufacturing, Mater. Sci. Eng. A., vol. 790, pp. 139743, 2020. DOI: 10.1016/j.msea.2020.139743.

[27] G. Cazzola, E. A. Razio, and F. Izquierdo, Study of the bending response of metal foam-filled beams applied to enhance the roll-over behaviour of coach structures, Int. J. Crashworthiness., vol. 18, no. 6, pp. 620–532, 2013. DOI: 10.1080/13588265.2013.831516.

[28] O. Al-Ketan, and R. K. Abu Al-Rub, MS Lattice: A free software for generating uniform and graded lattices based on triply periodic minimal surfaces, Mater. Des. Process. Commun., vol. 3, pp. 1–10, 2020.

[29] N. Novak, et al., Quasi-static and dynamic compressive behaviour of sheet TPMS cellular, Compos. Struct., vol. 266, pp. 113801, 2021. DOI: 10.1016/j.compstruct.2021.113801.

[30] N. Novak, M. Vesenjak, L. Krstulović-Opara, and Z. Ren, Mechanical characterisation of auxetic cellular structures built from inverted tetrapods, Compos. Struct., vol. 196, pp. 96–107, 2018. DOI: 10.1016/j.compstruct.2018.05.024.

[31] M. Borovinšek, PrePoMax. [Online]. Available: https://prepomax.fs.um.si/.

[32] J. Hallquist, LS-DYNA Keyword User's Manual, Livermore, CA: Livermore Software Technology Corporation, 2007.

[33] X. Li, C. C. Roth, T. Tancogne-Dejean, and D. Mohr, Rate- and temperature-dependent plasticity of additively manufactured stainless steel 316L: Characterization, modeling and application to crushing of shell-lattices, Int. J. Impact Eng., vol. 145, pp. 103671, 2020. DOI: 10.1016/j.ijimpeng.2020.103671.

[34] P. J. Blau, Friction Science and Technology, CRC Press, Florida, USA, 2008.

[35] Y. Wu, J. Fang, Z. Cheng, Y. He, and W. Li, Crashworthiness of tailored-property multi-cell tubular structures under axial crushing and lateral bending, Thin-Walled Struct., vol. 149, no. January, pp. 106640, 2020. DOI: 10.1016/j.tws.2020.106640.